CHARACTERISTICS OF SELF-EXCITED WAVE PROPAGATION IN A NON-PREMIXED LINEAR DETONATION COMBUSTOR

by

Deborah R. Jackson

A Thesis

Submitted to the Faculty of Purdue University

In Partial Fulfillment of the Requirements for the degree of

Master of Science in Mechanical Engineering

School of Mechanical Engineering

West Lafayette, Indiana

May 2022

THE PURDUE UNIVERSITY GRADUATE SCHOOL
STATEMENT OF COMMITTEE APPROVAL

Dr. Carson D. Slabaugh, Chair

School of Aeronautics and Astronautics

Dr. Carlo Scalo

School of Mechanical Engineering

Dr. Terrence R. Meyer

School of Mechanical Engineering

Approved by:

Dr. Nicole Key

To my Savior, Jesus Christ, and my fiance, Andrew Sebeny, and my parents, Jeff and Bev Jackson.

ACKNOWLEDGMENTS

First, I would like to thank my advisor Prof. Carson D. Slabaugh. He provided me with the incredible opportunity to be apart of a world-class group that conducts relevant and profound research. His support and guidance inspired me to push myself beyond my abilities and to work my hardest. Thanks to Prof. Carlo Scalo and Prof. Terrence R. Meyer for their willingness to serve on my advisory committee.

I would also like to thank my High Pressure Lab (HPL) colleagues. Particularly, Dr. Rohan Gejji, Dr. Kyle Schwinn, and Mark Frederick deserve my gratitude for their mentorship and patience. Not only did they help me conduct experiments and then analyze the resulting data, they were always available to answer my questions no matter how simple. Specifically, Dr. Gejji took great lengths to ensure my understanding and success. For that, I will always be grateful. Thanks to Zachary Ayers for his help processing phase averaged images and Dr. Ian Walters for his assistance in processing y-t plots. I am thankful to machinist Rob McGuire for his role in fabricating components for my experiment and for his advise that has made me a well-rounded engineer. Additionally, thanks to Allyson Haynes, Hannah Schenck, Alexis Harroun, Ariana Martinez, and Dr. Jenna Humble for their encouragement over coffee every Thursday morning.

I'd like to give special thanks to my parents, Jeffrey and Beverly Jackson, for their unconditional love and support. They have always been and will always be my most influential mentors. Lastly, special thanks to my fiance, Andrew Sebeny, for his inexhaustible support and love. He encouraged me to fight for my goals and believed in my abilities even when I didn't believe in myself. I am grateful for my family and friends who faithfully reminded me to rely on my Savior, Jesus Christ, to accomplish His work through me.

The high-speed cameras used in this work were purchased with DURIP grant FA9550-16-1-0534 from Dr. Chiping Li. I would like to thank him, Jason Burr, and John Bennewitz from the Air Force Office of Scientific Research (AFOSR) for their advise throughout the testing and analysis of this work under grant FA9550-21-1-013.

TABLE OF CONTENTS

LIST OF TABLES

LIST OF FIGURES

LIST OF SYMBOLS

α_r	coefficient of reflection
$^\circ$	degree
Δ_{rec}	fuel jet recovery time
Δ_{ref}	reflection time
$\varnothing$	diameter
f_c	cycle frequency
G	mass flux
$\dot{m}_{GOX}$	gaseous oxidizer mass flow rate
m/s	meters per seconds
$\%$	percentage
P'_{max}	maximum pressure fluctuation
ϕ	equivalence ratio
$r_{1,2}$	relative characteristic impedance
W	width
X	x-location
Y	y-location

ABBREVIATIONS

AFOSR	Air Force Office of Scientific Research
atm	standard atmosphere
BC	boundary condition
CEA	NASA chemical equilibrium application
CJ	chapman-jouguet maximum detonation wave speed
CL	chemiluminescence
CMOS	complementary metal oxide semiconductor
DDT	deflagration-to-detonation transition
HF	high frequency
HPL	high pressure lab
Hz	hertz
K	kelvin
kHz	kilohertz
KL	kulite piezoresistive pressure transducer
LDC	linear detonation combustor
MHz	megahertz
MPa	megapascal(s)
mm	millimeter(s)
ms	millisecond(s)
μs	microsecond(s)
NASA	National Aeronautics and Space Administration
NG	natural gas
OH*	hydroxyl radical
P	pressure
PCB	piezoelecric pressure transducer
PLIF	planar laser induced fluorescence
PMT	photomultiplier tube
PSD	power spectral density

RDE	rotating detonation engine
PSD	power spectral density
RTV	room temperature vulcanizing silicone
T	temperature
UV	ultraviolet

ABSTRACT

The interaction and behavior of detonation waves propagating in a linear detonation combustor (LDC) were studied to identify the coupled thermoacoustic-chemical phenomenon responsible for self-generated and self-sustained detonation waves. The LDC was operated with natural gas and gaseous oxygen over a wide range of equivalence ratios and optically observed with OH*-chemiluminescence, schlieren, and broadband imaging in addition to high-frequency pressure transducers and photomultiplier tubes. Counter-propagating, self-sustained detonation waves were observed in the semi-bounded combustor to accelerate and amplify consistently from the closed-boundary to the open-boundary. The incident waves then reflect off of the open-boundary and transition into weaker waves that propagate acoustically relative to the burned products before being reflected by the closed-boundary and accelerating to dominancy once again. The combustor was then modified to have symmetric boundary conditions with both ends closed. For closed cases, the detonation waves experienced similar acceleration and amplification processes. The incident waves accelerate until they are reflected by a closed boundary into a flow field for which the fuel-injectors have yet to recover. For this reason, the reflected waves propagate through burned products until they encounter fresh reactants and accelerate again. The closed boundary conditions also caused the direction of dominance to periodically alternate. This study indicates that the local mixing field between open and closed boundary conditions affects the strength and speed of the reflected wave and demonstrates the impact of combustor geometry on coupled thermoacoustic-chemical phenomenon in RDEs.

1. INTRODUCTION

1.1 Motivation

Propulsive devices that utilize pressure gain combustion are a promising alternative to traditional deflagration-based engines because of an increase in thermal efficiency from detonations [1]. Such detonative devices include rotating detonation engines (RDE's) which utilize an annular combustion chamber wherein transverse detonation waves propagate [2]. For RDE's, only one detonation wave is introduced into the system to initiate combustion and establish limit cycle behavior. Thereafter, reactants are introduced into the combustor and are consumed by continuously self-exciting detonation waves propagating in the channel. Detonations occur at near-constant volume and constrict the expansion of burned product gases which increases the cycle-averaged total pressure [3], [4]. This increase in total pressure results in an increase in thermal efficiency as much as 7% compared to gas turbine engines and deflagration-based rocket engines [5], [6]. Therefore, the complex driving-mechanisms that sustain RDE's should be further explored.

1.2 Background

Since pressure gain combustion utilizes detonations, which travel faster than deflagrative combustion waves, the reactant mass consumption increases and consequently, the thermal power density increases [7]. A detonation is a shock-coupled combustion front that is followed by compression and heat release. Reactants are ignited by adiabatic compression at the leading shock and then rapidly dissociated in the induction zone behind the front. Since the shock front travels supersonically relative to the local flow field, the gases behind the induction zone are unable to expand fast enough and form the combustion zone. The gases rapidly recombine causing strong local compressions and an increase in total pressure [8] in this zone producing a greater rate of enthalpy conversion with lower entropy generation than constant pressure combustion processes, such as deflagration. This conversion process also leads to a greater rate of mass consumption and consequently, increases the thermal power density of heat addition [8] and can lead to improvements in the thermodynamic efficiency

[5]. The shock front continues to travel supersonically as the pressure in the burned products begins to decrease and the local particle velocity declines to form expansion waves and in return, propel the shock front forward to sustain the detonation wave.

A real detonation wave in an RDE is composed of multiples structures as seen in Figure 1.1 [9]. Real detonation waves propagate along the injection surface with an attached oblique shock. The oblique shock is produced by the differential density between the layer of burnt products from the previous wave and the supersonic detonation front [10]. Because the layer of burnt products is relatively inert compared to the supersonic detonation front, a slip line is formed at the intersection of these two structures [11]. After the passage of a detonation front, a region of vortex-shedding develops between the fresh reactants and burned products due to the differences in density and temperature [12], [13]. Reactants are continually injected into the combustor and drive burned products out of the combustor as the next wave approaches.

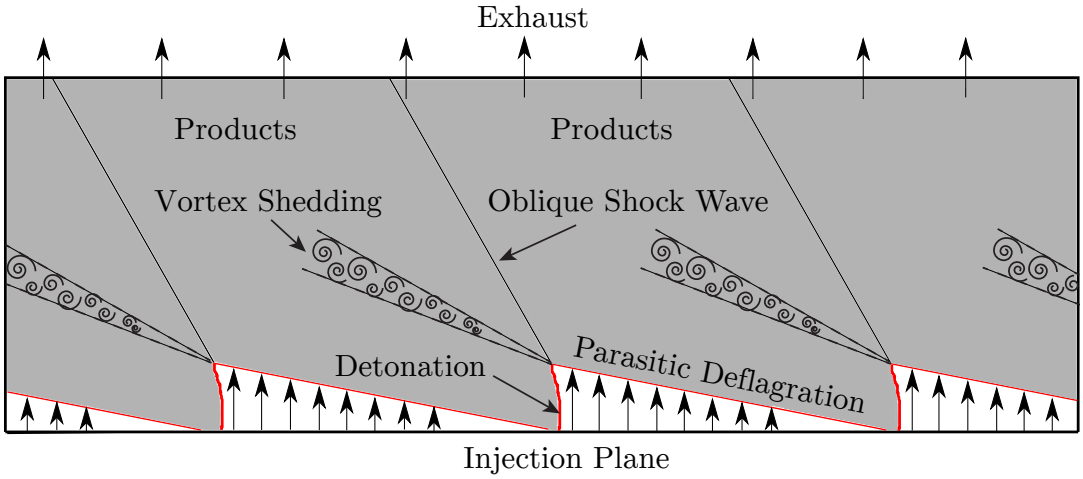

Figure 1.1. Schematic diagram of a linear detonation combustor during limit-cycle behavior (Reprinted from Ref. [9] with permission from authors).

Previous experimental observations of RDE's have established a wide range of detonation wave behavior. To explore the underlying mechanisms that drive these behaviors, the potential sources of instabilities have been investigated. Global gain dynamics such as injection [14], combustion timescales, exhaust process, and mixing [15] may amplify into instabilities. Pulsations from flame instabilities gradually transition into transverse waves which either

travel as deflagrations or detonations [16]. A combustion wave that transitions into a detonation wave either 1) rapidly accelerates to a steady velocity near the Chapman-Jouguet (CJ) value, 2) gradually accelerates to CJ, 3) becomes an overdriven detonation that decays and then is overdriven again, or 4) decelerates and decays into a blast wave [17]. However, detonations and deflagrations can coexist within the same reactive system and propagate according to multiple modes [16]. In an LDC, four modes have been established as 1) only deflagrative combustion, 2) one single detonation wave, 3) two counter-propagating detonations waves, and 4) a single strong wave propagating counter to a single weak wave [18]. Typically, the number of waves is established by the interaction of a wave with a counter-propagating wave which increases the local pressures and temperatures [19] and consequently, slows the propagation of the dominant wave. The dominant wave then elongates and gradually splits into two new waves [20]. Correlations between the number of waves present in a device and the mass flow rate [21] and the equivalence ratio [18] have been established. The mixture influences the ignition timescales which affects the separation rate and induction length and, ultimately, impacts the cell size [22].

Geometric features such as boundary conditions are very influential for detonation behavior within RDE's. Temperature fluctuations, referred to as entropy waves, result from thermoacoustic instabilities and emit acoustic waves [23]. These acoustic waves that are generated by flame propagation reflect off of walls and other geometric features inherent to the combustor. The reflected acoustic waves then interact with the flame front and develop flame perturbations as a result of instability mechanisms [24]. Simply, acoustic waves interact constructively and destructively with backward acoustic waves formed by the reflection of these waves from choked boundary conditions to create turbulence and noise which can grow non-linearly [25]. Acoustic waves then interact with chemical kinetic processes in a nonlinear coupled manner that can alter the behavior of the combustor by emitting undesirable frequencies [26]. Severe flame distortion may occur from this interaction which will, consequently, increase the flame front surface area, volumetric burning rate, and flame velocity. If the propagating flame is travelling at a sufficient velocity, this interaction may cause a deflagration-to-detonation transition (DDT) [3], [24]. This process will create more

instabilities and turbulence in the flame and the cycle will repeat itself as to sustain the limit-cycle behavior of the combustor.

1.3 Objective

In this work, the author seeks to develop a detailed understanding of the mechanisms of acceleration and amplification for waves in a non-premixed linear detonation combustor. High-speed optical diagnostics and high-frequency sensors were deployed in an LDC of differing geometric configurations to explore the characteristics of detonation waves throughout the combustor. The influence of combustor geometry on wave acceleration, amplification, and self-excitation is the focus of this discussion.

2. EXPERIMENTAL DESCRIPTION

2.1 Hardware

For this work, all experiments were performed in a linear detonation combustor that imitates an annular RDE chamber in a linear test section to maximize high-speed diagnostics. Figure 2.1 depicts key geometric features and dimensions of the experiment. The combustor is operated with natural gas (NG) as the primary fuel for its relatively low cost and easy accessibility. The natural gas consists of methane (85.63%), ethane (11.26%), nitrogen (2.06%), propane (0.83%), and carbon dioxide (0.79%) [27]. To ensure detonability, oxygen serves as the oxidizer. As seen in Figure 2.1b, oxygen is delivered to the chamber through a 0.76 mm wide slot axial injector spanning the full transverse (Y-direction) length of the chamber. Natural gas is injected from alternating sides of the oxidizer slot from evenly spaced, discrete fuel injectors, 1.27 mm in diameter. Fuel delivered from these injectors impinge on the oxidizer sheet at 30° relative to the axial (X-) direction of the combustion chamber. The combustion chamber width was selected to support characteristic detonation cell size produced by natural gas-oxygen detonations at near ambient pre-ignition conditions. The reactant injection system is sized to promote critical flow between each detonation wave passage at all operating conditions and prevent flash-back which is a common issue for premixed experiments [28]. Choked orifices are installed at each reactant manifold inlet to enable acoustic isolation of the highly dynamic conditions present within each manifold from facility fluid systems. Additionally, these orifices provide well-defined acoustic inlet boundary conditions for comparison with computational modeling efforts. They possess a sufficiently high pressure ratio to adequately isolate combustion chamber dynamics from the reactant feed-system and vice versa. Combustion products are exhausted through downstream axial and transverse exit boundaries. These boundaries are exposed to ambient conditions except some cases for which a stainless-steel plate is installed at the upstream (Y = 540 mm) transverse end of the combustion chamber to enforce a closed boundary condition.

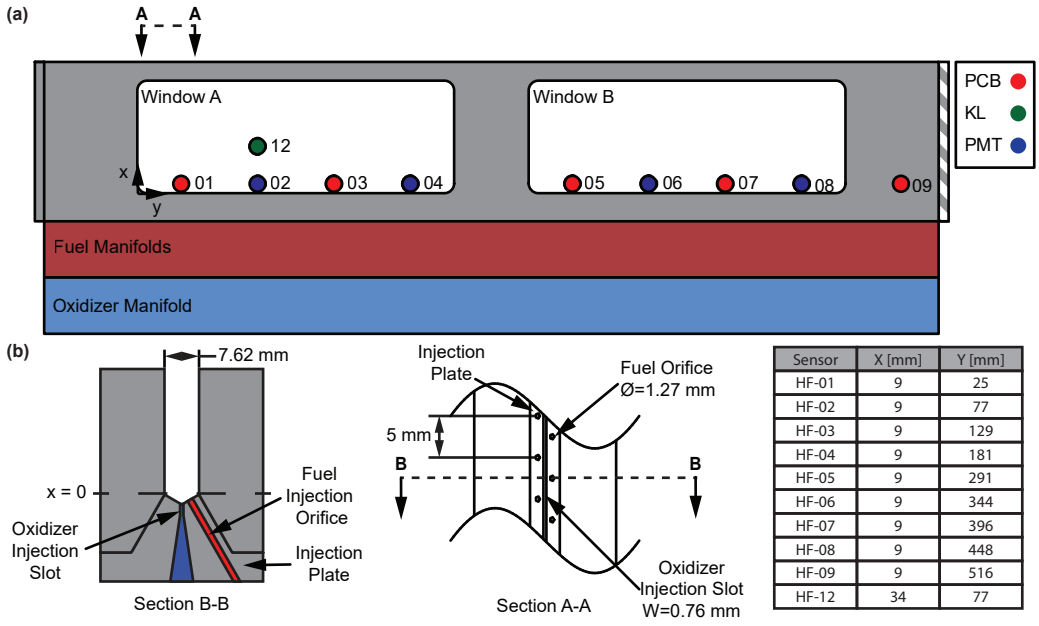

Sensor	X [mm]	Y [mm]
HF-01	9	25
HF-02	9	77
HF-03	9	129
HF-04	9	181
HF-05	9	291
HF-06	9	344
HF-07	9	396
HF-08	9	448
HF-09	9	516
HF-12	34	77

Figure 2.1. (a) Optical-access and probe-based instrumentation installation locations for each reactant manifold and combustion chamber. (b) Schematic representation of the fuel an oxidizer injection scheme.

2.2 Instrumentation and Optical Diagnostics

Fused quartz windows are installed to provide a 215 mm x 76 mm field of view for high-fidelity diagnostics in the combustor as seen in Figure 2.1a. Instrumentation blanks are installed transversely to the windows for high-frequency, probe-type instrumentation to acquire wall pressure measurements at a sampling rate of 2 MHz and inform the wave behavior observed optically. Such instrumentation includes piezoelectric pressure transducers (PCB 133B26), piezoresistive pressure transducers (Kulite WCT312M), and photo-multiplier tubes (PMT) as called out in Figure 2.1a. The PCB's measure the pressure fluctuation throughout the combustor while the Kulite measures absolute pressure. The PMT's are filtered to measure the light emitted by the combustion front that corresponds to the wavelength of hydroxyl (OH*) radicals. These instruments are flushed-mounted as to not intrude upon the chamber dynamics while maintaining accuracy [29].

To characterize primary factors that impact the wave behavior in the combustor, high space-time resolution measurements are performed in the window A region using simultane-

ous 96 kHz schlieren and OH*-chemiluminescence measurements as depicted in Figure 2.2a. OH*-chemiluminescence images are obtained with a Complementary Metal Oxide Semiconductor (CMOS) camera (Phantom v2512) and a UV filter (Semrock FF02-320/40) centered at 320 nm with a bandpass of 40 nm. These images are collected with a UV lens (98 mm Nikon f/2.8) at a focal length of 98 mm and amplified with an intensifier (Lambert HiCatt, S25 microchannel plate). A 1μs exposure time is used to ensure sufficient signal collection for each frame with a 207 mm x 82 mm field of view and resolution of 3.7 pixel/mm.

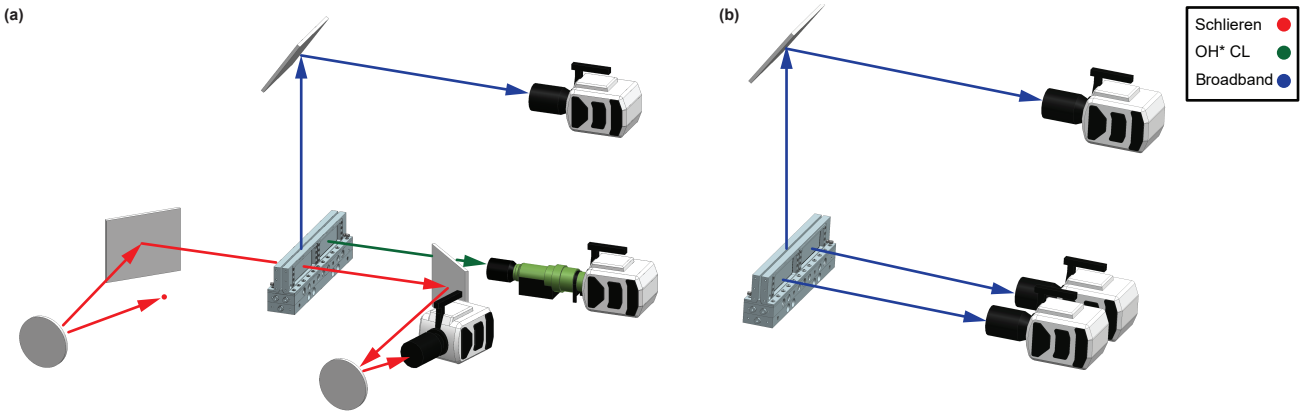

Figure 2.2. (a) Schematic representation of the first optical diagnostic configuration which includes OH*-Chemiluminescence (green) and schlieren (red) imaging of Window A and aft-end broadband imaging (blue). (b) Schematic representation of the second optical diagnostic configuration which includes broadband imaging (blue) of Window A, window B, and the aft-end.

A z-type schlieren setup is used for measurements of density gradients in the flow to characterize the detonation front [30], [31]. A high-repetition rate light source was developed for the schlieren measurements. As seen in Figure 2.2a, the light source expands until it is colluminated by a parabolic mirror. The column of light then reflects off of a planar mirror through the combustor to another planar mirror. The image travels to a second parabolic mirror that decolluminates the light. A knife edge is placed at the focal point, approx. 2 meters from the parabolic mirror, to cut the image in half. After the knife edge, a second Phantom v2512 camera with a 250 mm lens is positioned to capture this image. This camera also operates at a sampling rate of 96 kHz with an exposure time of 9.5 μs and resolution of 3.4 pixel/mm for a 225 mm x 89 mm field of view.

Broadband images of the aft-end of the experiment are also recorded at 96 kHz to document the temporal and spatial history of waves propagating along the full length of the combustor. This perspective provides insight into combustor behavior beyond the limitations of the fused quartz windows and grants a new path for which optical diagnostics are integrated. This camera has an exposure time of 1 μs, a 1.09 pixel/mm resolution, and a 557 mm x 51 mm field of view.

A second diagnostic configuration is depicted in Figure 2.2b. Broadband images of the aft-end, window A, and window B are obtained simultaneously at a sampling rate of 96 kHz. Both broadband images in window A and B are obtained with a CMOS camera (Phantom v2512) while the broadband images of the aft-end are captured with a CMOS camera (Phantom v411). All cameras are spatially calibrated with a 3-D calibration plate (LaVision Type 058-5) and LaVision DaVis software.

2.3 Experimental Modifications

To characterize wave initiation and propagation in the LDC through targeted tests, the experiment has been modified to extend the window A closed boundary condition to move the circulation zone into an optically accessible region of the experiment. This zone could not be observed in previous configurations studied by Schwinn et al. [9], [30], [32] due to optical obstruction to the left of window A. To relocate this circulation zone, stainless steel blocks were placed in the manifolds, injection plate, and combustion chamber.

As seen in Figure 2.3a, an insert was placed in the oxidizer manifold and fixed in position with a 3.2 mm rod inserted through the instrumentation port on the left-hand side of the manifold. A 0.8 mm thick Viton rubber pad was then placed on top of the insert to eliminate excess gap during assembly. An insert was also positioned in the oxidizer slot that passes between the two fuel manifolds and held in place with compression between the Viton pad below and the insert in the injector plate above. This third insert was placed in the injector plate to block the discrete slot that injects the oxidizer into the combustion chamber. It was also held in position by compression between the slot insert below and the injection plate above.

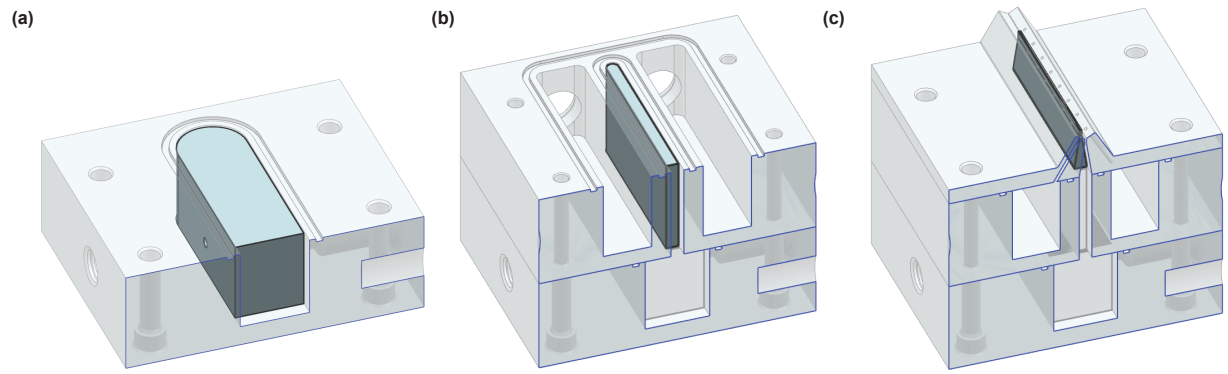

Figure 2.3. (a) Stainless steel insert in Gox manifold, (b) in Gox slot between fuel manifolds, and (c) in Gox slot in injector plate.

Likewise, stainless steel inserts were placed in the fuel manifolds and discrete orifices as depicted in Figure 2.4. An insert was fixed in each fuel manifold with a 3.2 mm thick Viton rubber pad under compression similarly to the insert placed in the oxidizer manifold. Downstream in the injection plate, fourteen stainless steel pins (seven on either side) with a diameter of 1.24 mm were utilized to plug the 1.27 mm diameter discrete fuel orifices. These pins were then sealed with room temperature vulcanizing (RTV) silicone that is resistant to high temperatures. The silicone was placed on the the bottom of the injection plate where the orifices interface with the fuel manifolds. The pins have a tapered head to fix their positions so the silicone was layered over the tapered heads.

A stainless steel insert was also placed in the combustion chamber as seen in Figure 2.5. This insert were fixed in place with two screws through the top of the insert into the combustor walls and six screws through the back of the insert into the walls. The sides of the insert were coated with a film of high-temperature RTV silicone to seal this corner in the combustor and force the circulation zone to be at the edge of window A. The insert overlaps the window's edge by 5.08 mm which is less than the window's corner radius of 6.35 mm. To re-create the circulation zone, the distance between the insert and the first injector element that is not blocked was maintained without permanently modifying the experiment.

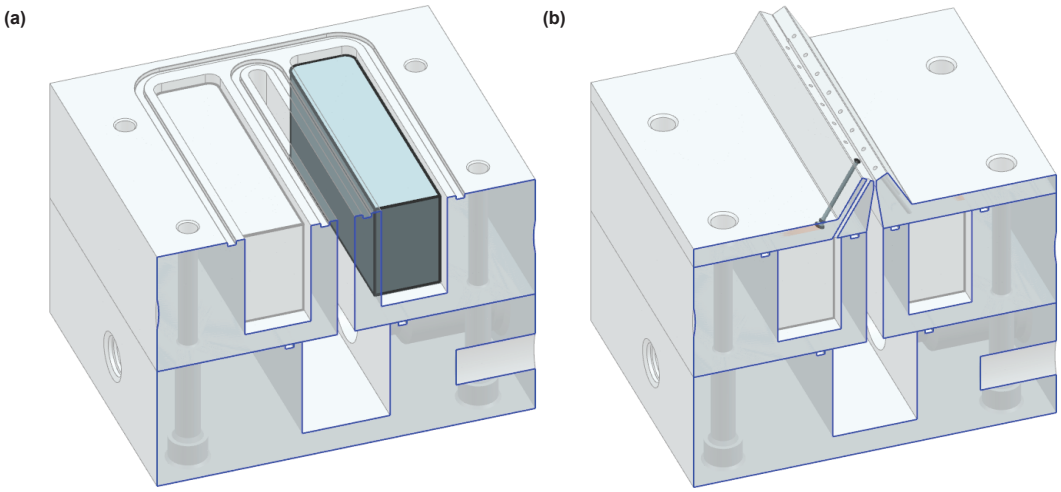

Figure 2.4. (a) Stainless steel insert in fuel manifolds and (b) stainless steel pins in fuel orifices of injector plate.

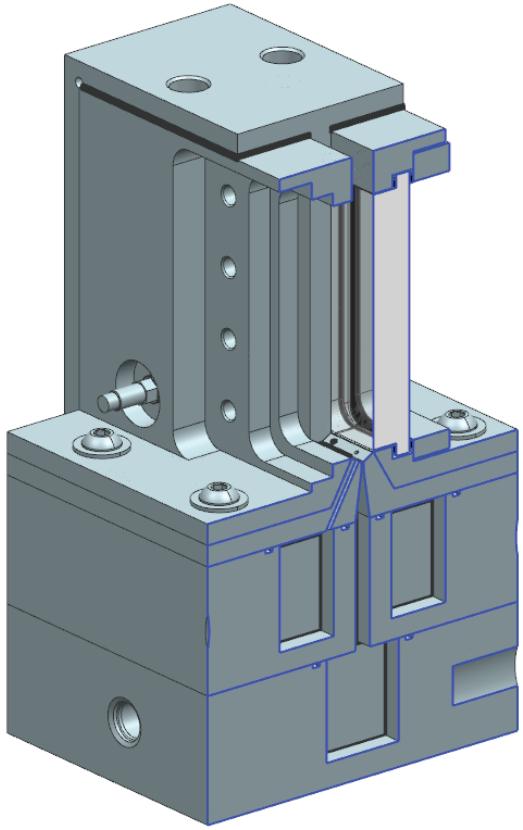

Figure 2.5. Stainless steel inserts in the oxidizer manifold, fuel manifolds, injection plate, and combustion chamber to relocate the circulation zone to the window A region.

2.4 Operation and Behavior

Combustion in this experiment is initiated with a spark-ignited pre-detonator of gaseous hydrogen and oxygen through a 4.57 mm tube into the combustor located at Y = 0 mm. Because the combustor and manifolds have been modified with stainless steel inserts to relocate the corner at Y = 0 mm to the left-edge of window A, the pre-detonator tube is located at the edge of window A downstream of the combustor. The tube is angled down at a 45 degree angle relative to the longitudinal (Y-) direction so that the edge of the tube is at the edge of the channel walls (X = 91 mm) to guide the initial pulse into the combustor. A y-t plot of this ignition process is presented in Figure 2.6a which is derived from the broadband images taken from the aft-end of the experiment similar those taken of RDEs [19], [33], [34]. Each dark line crossing the length of the combustor, referred to as a "streak", is the temporal and spatial history of a propagating combustion wave in the combustor. As seen in Figure 2.6a, the pulse emanates from the pre-detonator and propagates from the ignition location (Y = 0 mm) to the open boundary (Y = 540 mm). A short transition period (approx. 1 ms) follows during which the limit-cycle instabilities from this initial pulse non-linearly amplify into periodic detonative behavior. Figure 2.6b presents the y-t plot for 18−22 ms after ignition during steady-state operation. Streaks with a positive slope represent combustion waves which travel across the combustion chamber from the left (Y = 0 mm) to the right (Y = 540 mm) end of the combustor and are referred to as right-running waves. Streaks with a negative slope propagate counter to the right-running waves and are referred to as left-running waves. During steady-state operation, periodic self-sustained detonations are self-excited at kilohertz rates [9] and the location of ignition doesn't impact this limit-cycle behavior [27].

This ignition process is observed by the HF pressure transducers placed in the combustor as seen in Figure 2.7. The pressure trace of the PCB installed in HF-07 has been passed through a high-pass filter to be de-trended during ignition and steady state operation before thermal saturation occurs. As presented in Figure 2.7a, the large rise in pressure aligns with the initial pulse generated by the pre-detonator in Figure 2.6a. After a short transition period, steep-fronted pressure fluctuations develop in the combustor and maintain cyclic

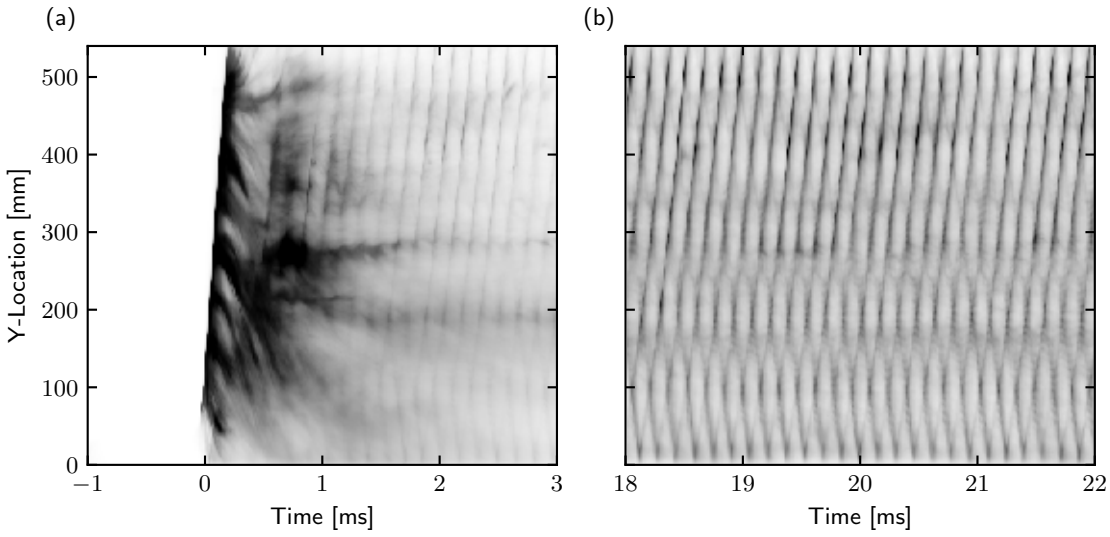

Figure 2.6. Y-t plot for fuel-lean case with an open boundary at (a) ignition and (b) steady-state operation.

behavior throughout steady operation as seen in Figure 2.7. The periodicity of the steep-fronted pressure spikes recorded by HF pressure transducers correspond to the combustion waves observed in Figure 2.6.

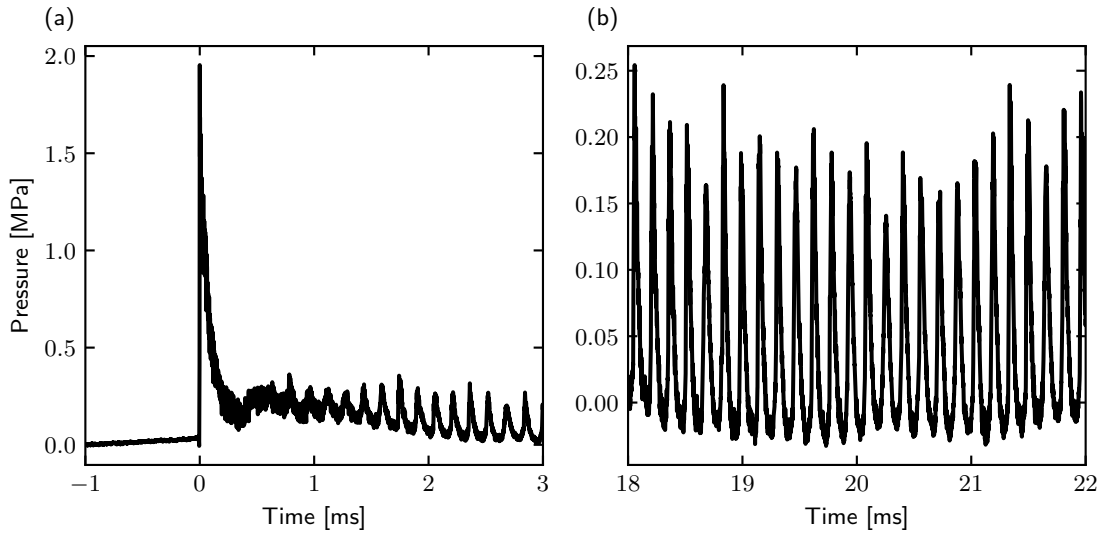

Figure 2.7. Pressure traces of PCB located at HF-07 at (a) ignition and (b) steady-state operation.

3. RESULTS AND DISCUSSION

3.1 Global Wave Dynamics

Self-excited and self-sustained combustion waves have been observed in this LDC during operation [9], [35], [36] but the presence of multiple self-excited, counter-propagating combustion waves have been discovered in the LDC under the operating conditions detailed in Table 3.1. These test cases were performed at an approximate mass flux, G, of 120 kg/m.s2 over a range of equivalence ratios, ϕ, and differing boundary conditions (BC) which describe the wall at Y = 540 mm. Cases with an open BC were conducted with no plate at Y = 540 mm while cases with a closed BC have a stainless steel plate fixed at the end. The mass flow rates for the oxidizer, $\dot{m}_{GOX}$, and fuel are controlled and metered with critical flow venturi nozzles [37] so that the targeted test conditions are met. The uncertainty in the mass flow rates and resulting conditions are computed with the Kline-McClintock method [38], [39]. A 95% confidence interval is applied to this value which results in an uncertainty that is less than 1% of the total mass flow rate for all cases [27], [40].

Table 3.1. Operating and boundary conditions of select test cases.

Case	ϕ	G $(\frac{kg}{s.m^2})$	$\dot{m}_{GOX}$ $(\frac{kg}{s})$	BC
(i)	0.80	122	0.417	*Open*
(ii)	1.02	118	0.385	*Open*
(iii)	1.20	119	0.373	*Open*
(iv)	0.78	122	0.417	*Closed*
(v)	1.02	118	0.385	*Closed*
(vi)	1.18	118	0.373	*Closed*

The observed cycle frequency and maximum pressure fluctuation, P'_{max}, for each case is presented in Figure 3.1. The maximum pressure fluctuation is determined from the PCB sensor located at instrumentation location HF-07 from 10 to 50 ms after spark ignition because instrument thermal saturation occurs after 50 ms for some cases. The pressure fluctuation is normalized with respect to the average pressure drop across the fuel injector. This normalization accounts for the dependence of fuel injector recovery time on the fuel

manifold dynamics, combustor cycle period, mean injector stiffness, and pressure fluctuation [36]. The cycle frequency, f_c, is calculated from the power spectral density (PSD) of this sensor in Figure 3.2 from 10 to 50 ms after spark ignition. To produce the power spectral density of this sensor, the corresponding pressure trace during steady state operation is placed into the frequency domain in a Hanning window and the resulting periodogram is filtered through a Welch Estimate to calculate the power of the frequencies present in the periodic behavior. The steep-fronted, cyclic pressure fluctuations presented in Figure 2.6b correspond to the greatest peak at 6.42 kHz in the PSD. The peak at approximately 450 Hz represents the fundamental transverse acoustic mode in the chamber while the two satellite peaks surrounding the cyclic peak (6.42 kHz) are observed at the sum-difference frequencies between the cyclic (6.42 kHz) and transverse (450 Hz) peaks. The presence of these peaks indicates that the fundamental acoustic mode is non-linearly interacting with the cyclic wave behavior in the combustor [9]. The frequency with the greatest power in this power spectral density plot, which is 6.42 kHz, is selected as the cycle frequency.

As seen in Figure 3.1, the frequency consistently increases as the equivalence ratio increases for all cases. Meanwhile, for open cases, the maximum pressure fluctuation is greatest at stoichiometric conditions and the fluctuation for closed cases maximizes at an equivalence ratio of 0.80.

As frequency increases with equivalence ratio, the number of detonation waves present in the combustor also increases as seen in Figure 3.3. The number of waves is calculated from the number of streaks present at any point in time in a y-t plot which is derived from the aft-end broadband imaging as seen in Figure 3.4. This value is then averaged over the duration of steady state operation since frequency negligibly changes with time throughout the test. For this sample, the number of waves present in the combustor is six since six streaks intersect with the vertical line at a give point in time during steady state operation. The uncertainty in this value is calculated with a 95% confidence interval and then averaged for temporal and spatial uncertainties in the original image and the blurring of this image as determined by the wave speed and exposure time [41]. The resulting uncertainty becomes less than 1 wave for each case. Because the frequency for this periodic behavior increases with equivalence ratio, the number of detonation waves generally increases. However, the

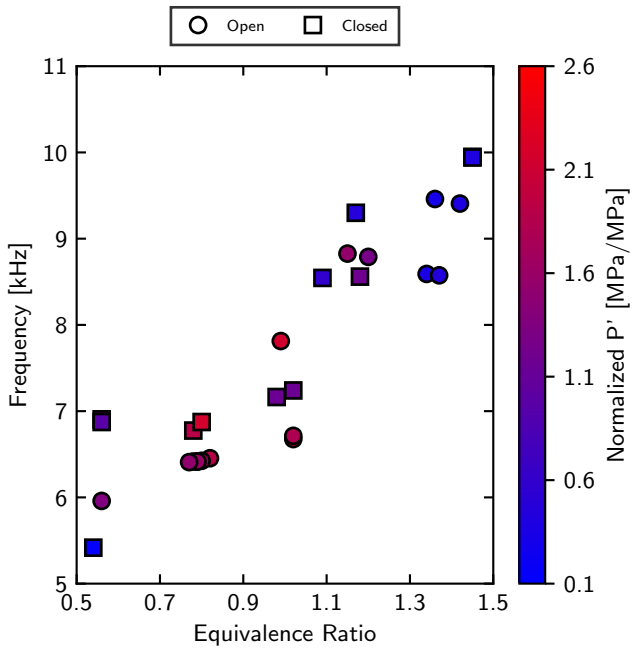

Figure 3.1. Frequency of steady-state behavior vs equivalence ratio vs normalized pressure fluctuation.

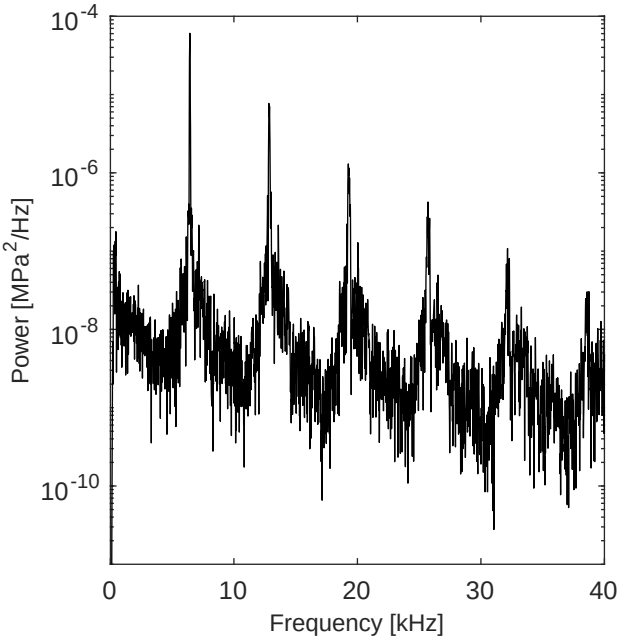

Figure 3.2. Power Spectral Density of PCB at location HF-07 during steady state operation.

number of waves minimizes at an equivalence ratio of 0.80 where the pressure fluctuation maximizes for closed cases. This trend indicates that one parameter doesn't linearly influence the other since additional coupled mechanisms such as wave speed and mixing are present.

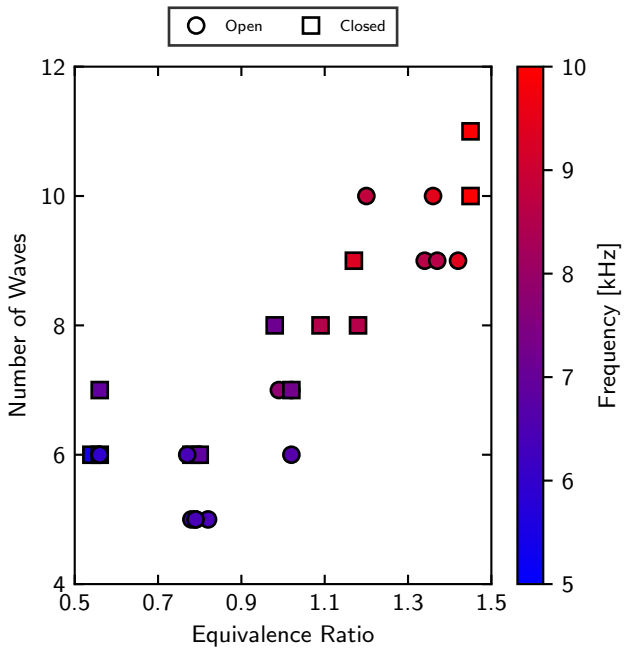

Figure 3.3. The number of waves vs equivalence ratio vs frequency.

3.1.1 Impact of Experimental Modifications on Global Wave Dynamics

To ensure that these global wave dynamics haven't been influenced by the modifications made to the experimental device as described in Section 2.3, these dynamics were compared to previous experiments for which the device wasn't modified. In Figure 3.5, the cycle frequency and normalized pressure fluctuation are presented for cases conducted in the original combustor with a Y-length of 610 mm and for cases in the modified combustor of 540 mm. For these cases, in both combustor configurations, the boundary at Y = 0 mm is closed and the other boundary (Y = 610 or 540 mm) is open. Because PCB transducers were not installed at HF-07 in the original configuration, the neighboring PCB installed at HF-08 was selected for these cases. The pressure fluctuation is normalized as previously discussed and its power spectral density is utilized to calculate the cycle frequency.

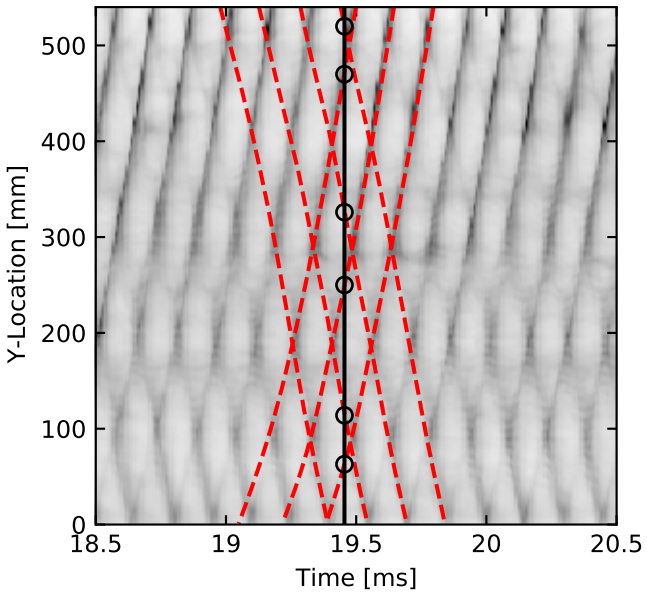

Figure 3.4. The number of waves present in the combustor as indicated by the number of streaks.

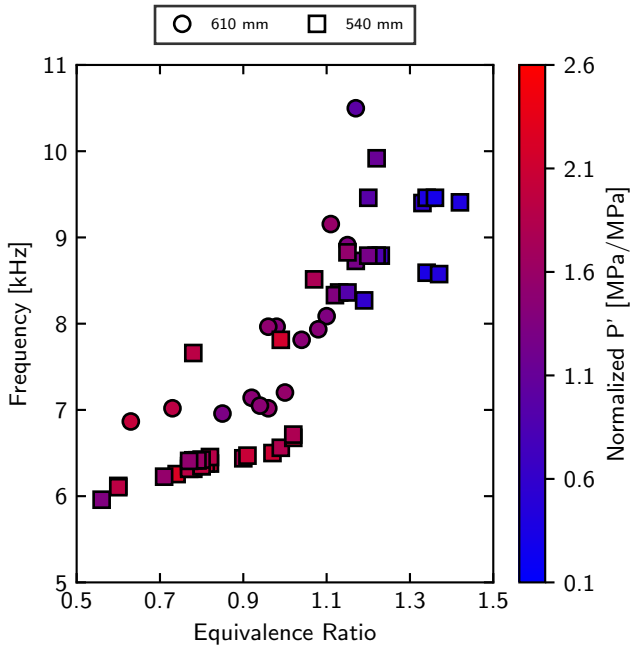

Figure 3.5. Comparison between the global wave dynamics of the modified (540 mm) and original (610 mm) combustor configurations with an open boundary.

As seen in Figure 3.5, the pressure fluctuation maximizes at an equivalence ratio of 0.80 for the original combustor and at 1.0 for the modified combustor. The frequency increases as equivalence ratio increases for both configurations but the shorter combustor experiences cycle frequencies approximately 500 Hz less than those of the longer combustor for fuel-lean cases. As the equivalence ratio transitions from fuel-lean to fuel-rich, the frequencies of both configurations converge. These slight discrepancies between pressure fluctuation and cycle frequencies don't prohibit the global limit-cycle behavior observed in the combustor. Therefore, the remainder of the results presented in this work are discussed under the assumption that the modifications made to this combustor don't impact the operation and behavior of the combustor.

3.2 Acceleration of Detonation Waves

To calculate the wave speed of the combustion waves in the combustor and quantify their acceleration and behavior along the length of the combustor, an algorithm was developed that utilizes the broadband images taken from the aft-end of the experiment downstream of the combustor.

3.2.1 Wave Speed Algorithm

The wave speed is calculated by tracking the wave fronts presented in Figure 2.6b. To isolate the wave speed for the left-running and right-running waves, the y-t plot from the aft-end broadband imaging is separated into two different y-t plots for each direction as seen in Figure 3.6a and 3.6b. The original y-t plot seen in Figure 2.6b is transformed into Fourier space and the theta angles corresponding to right-running waves (positive) are formed by removing the theta angle modes for the left-running waves (negative) and vice versa. The theta angles are then transformed back into physical space to create the y-t plots for the left-running waves in Figure 3.6a and right-running waves in 3.6b.

To trace the contour of the detonation wave front in each y-t plot, a marching square algorithm is employed to target dark regions as seen in Figure 3.6c and 3.6d. Marching squares parses through each pixel in the image and sets pixels that possess a value greater

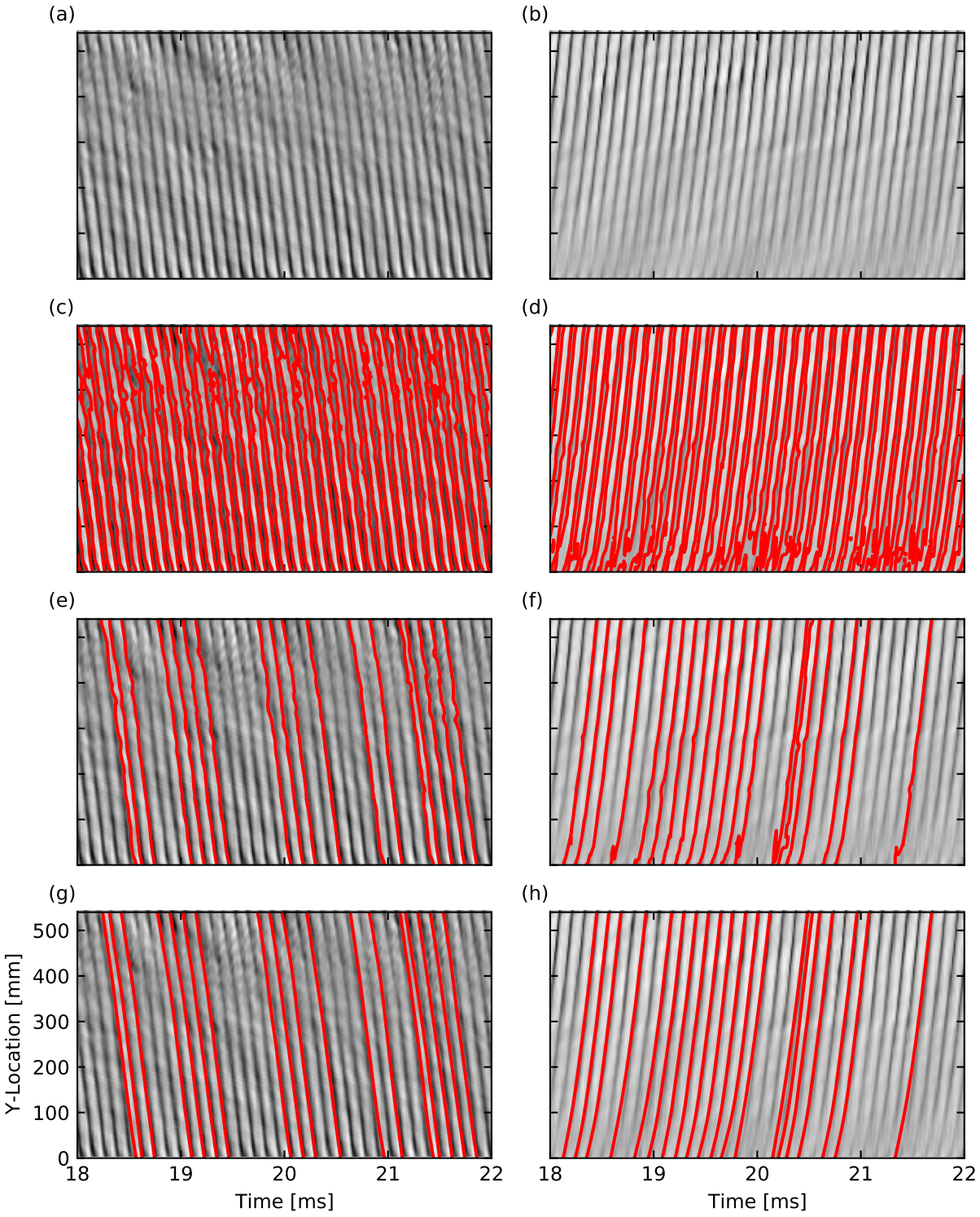

Figure 3.6. Step-by-step process for acquiring wave speed.

than the targeted value to "True" and all other pixels to "False". A mesh of squares is formed so that each corner is defined by the center of a pixel. Each square is ascribed a case according to the Boolean values of the corners. These assigned cases are then linearly interpolated with the values in the original image to find the edges present in the image.

Since the marching squares algorithm only detects edges present in an image and isn't capable of discriminating which edges fall on the front of the detonation wave, each contour is split into two contours so that they no longer "wrap" around each streak. A Sobel filter is applied to the y-t plot before finding the intensity peaks for each wave at a given y-location. The half of the contour that falls closest to these peaks are selected as the detonation fronts as seen in Figure 3.6e and 3.6f.

The marching squares contours along the detonation fronts are then utilized as an initial guess for an active contour "snake" model to search for curves and edges in the original image. The resulting, smoothed wave fronts are presented in Figure 3.6g and 3.6h.

From the slopes of the smoothed wave fronts, the instantaneous wave speed for each wave along the length of the combustor is calculated and presented in Figure 3.7. The speed of right-running waves are depicted in the positive region while the left-running waves' velocities are in the negative region for 4 ms of steady operation.

Finally, in Figure 3.8, the average wave speed is determined by averaging these velocities temporally along the length of the combustor. The wave speed temporally averaged over the 4 ms window for the combustion waves travelling rightward is represented by the solid line in the positive quadrant while that of the counter-propagating waves travelling leftward is in the negative region. The grey region surrounding the averaged wave speed represents the minimum and maximum variation in speed of any wave at any time travelling in that direction at that y-location. The right-running waves accelerate and become supersonic relative to both fresh reactants and burned products as determined by NASA Chemical Equilibrium Application (CEA). The acoustic speed of fresh reactants is between 350 and 360 m/s while the maximum acoustic velocity of the burned products is between 1240 and 1360 m/s for lean and rich cases, respectively. The more conservative estimate between the two values is that of the burned products so it is selected as the criterion for comparison in this work.

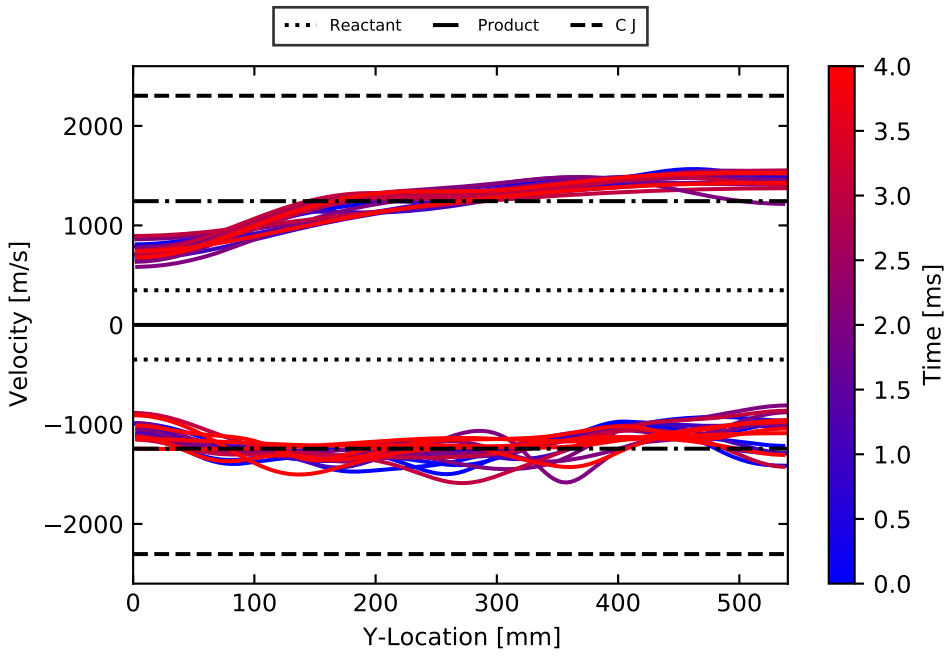

Figure 3.7. The instantaneous wave speed for each left-running (negative) and right-running (positive) wave.

The uncertainty in the average wave speeds has a 95% confidence interval that is applied to the root sum of squares of uncertainties. Such uncertainties include the temporal and spatial uncertainties in the original image and image blurring as determined by the wave speed and exposure time [41]. Additionally, the uncertainty in this post-processing methodology is defined by the temporal and spatial standard deviations and are included in the sum of uncertainties. The resulting uncertainty in wave speed is between 10 and 50 m/s for each case.

3.2.2 Wave Speed Results

The self-excited combustion waves accelerate along the length of the LDC before being reflected by boundary conditions for each case as demonstrated by the average wave speeds presented in Figure 3.9. The right-running combustion waves become supersonic, conservatively, after travelling between 200 and 400 mm and then continue to accelerate. Fuel-lean cases (black) accelerate faster than fuel-rich cases (blue) which indicates that as the equiva-

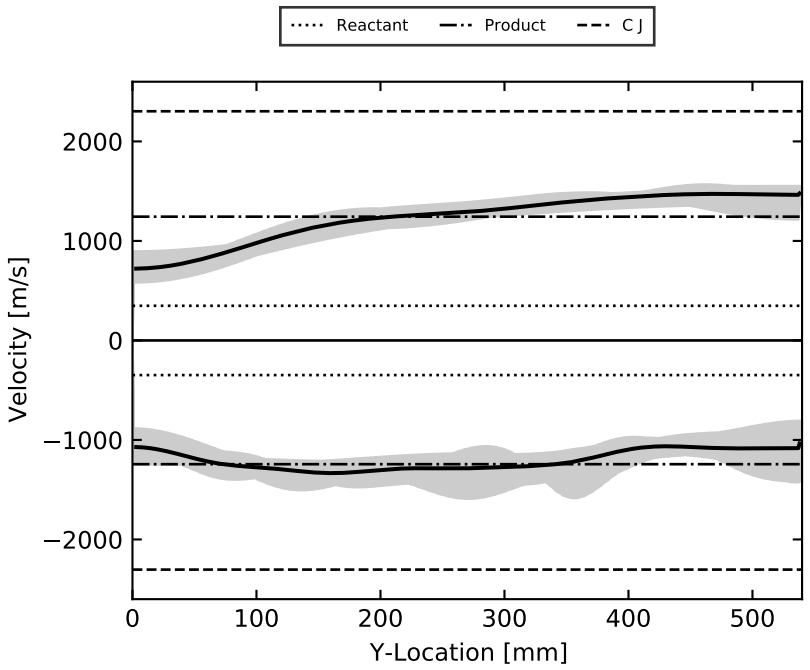

Figure 3.8. The averaged wave speed for each left-running (negative) and right-running (positive) wave.

lence ratio increases, causing the frequency and number of waves to increase, there are more detonation waves "competing" for fresh reactants to consume. As a result, the detonation waves in fuel-rich cases are not able to accelerate as quickly as those in fuel-lean cases which have more fresh reactants for each individual wave to consume.

These rightward travelling detonation waves then reflect off the boundary condition and transition into left-running waves. For open cases, the left-running waves travel acoustically relative to the burned products while those in closed cases accelerate but never become supersonic. In closed cases, the left-running waves travel at a lower speed in the window B region compared to those in open cases because the right-running wave is immediately reflected into a flow field that has yet to recover and is filled with burned products.

The period between the right-running detonation wave and the reflected wave determines the constituents available for the wave to consume as seen in Figure 3.10. The period between the incident wave and the reflected wave is defined as the time between the passage of the right-running wave at the end of the combustor (Y = 540 mm) and the entrance of the left-

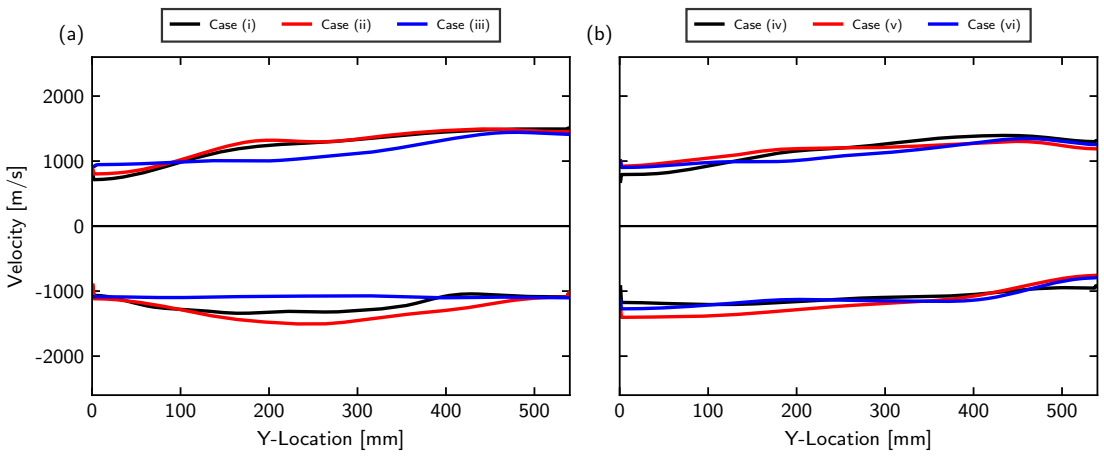

Figure 3.9. Combustion waves travelling rightward (positive) accelerate and reflect to become left-running waves (negative) for (a) open and (b) closed cases.

running wave at the same y-location. A 95% confidence interval uncertainty is calculated for the average reflection time, Δ_{ref}, considering temporal and spatial uncertainties in the original frames and image blurring caused by both the right-running and left-running waves at this y-location. The detonation wave fronts are highlighted by red, dashed lines overlaid onto the corresponding y-t plots where positively-sloped lines follow right-running waves and left-running waves have negative slopes. For the open case in Figure 3.10a, there is a delay between right-running combustion waves (positive slope) and leftward travelling waves (negative slope) that is not present for the closed case in Figure 3.10b.

The time delay between the passage of the right-running and the arrival of the left-running wave must be longer than the injector recovery time for the fuel and oxidizer to encourage the propagation of the left-running wave. The fuel jet recovery time, Δ_{rec}, for this combustor has been quantified with acetone-PLIF for open cases with comparable equivalence ratios [35], [36] as presented in Table 3.2. The fuel jet recovery time decreases as equivalence ratio increases [35] because fuel-rich cases have higher fuel injection pressure than fuel-lean cases [9]. Meanwhile, the oxidizer injector has a longer recovery time than the fuel injector but is independent of equivalence ratio [35]. As a result, there is ample time for the injectors in open cases to recover after the passage of the incident wave before the reflected wave arrives. However, the closed cases reflect the right-running wave immediately off the stainless steel

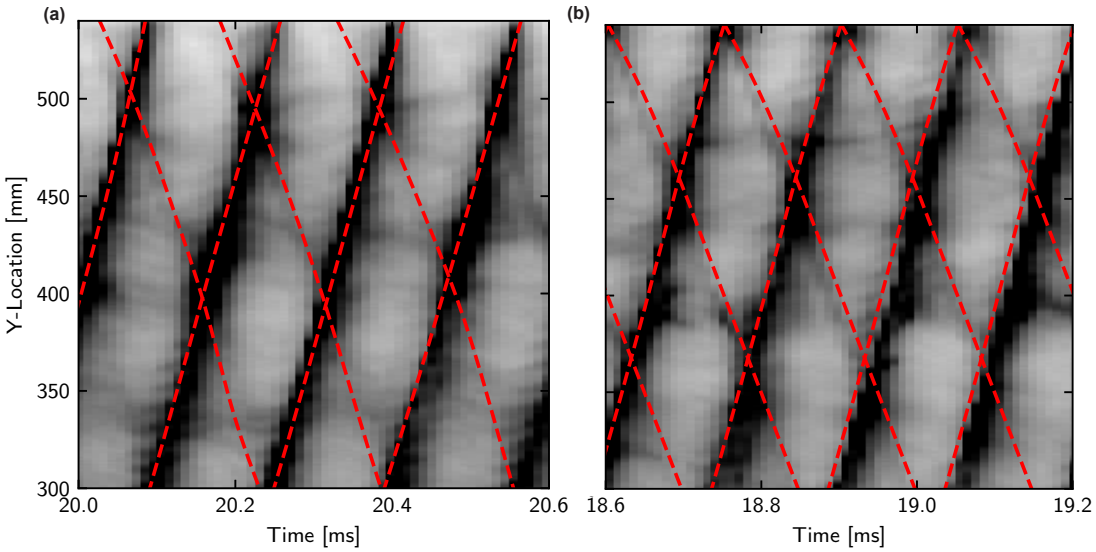

Figure 3.10. (a) zoomed-in y-t plot from case (i) with closed-open BC to exhibit time delay between right-running detonation waves and reflected combustion waves. (b) zoomed-in y-t plot from case (iv) with closed-closed BC to exhibit no time delay.

plate which is not enough time for the injectors to recover. This lack of sufficient time delay means that the now left-running wave propagates through the products burned by the right-running wave. These left-running waves propagate slower and emit less light intensity since they are unable to consume and combust as many reactants as the dominant right-running waves.

Table 3.2. Fuel jet recovery time and reflection time for each open case.

Case	ϕ	Δ_{rec} (μs)	Δ_{ref} (μs)
(i)	0.80	24	68 ± 3
(ii)	1.02	18	61 ± 2
(iii)	1.20	14	60 ± 2

This trend is consistent for both closed-boundaries in the closed cases and for the closed boundary at Y = 0 mm in open cases as seen in Figure 3.9. At all closed boundaries the incident detonation wave is reflected immediately into the burned products before the injectors are able to recover. As a result, the velocity of the right-running wave is less

than that of the left-running wave after it reflects at Y = 0 mm for both open and closed cases since the boundary at the left end is enclosed by a stainless steel plate. Similarly, the wave speed decreases after being reflected at Y = 540 mm but the difference in velocity between the right-running and left-running waves at this boundary is greater for the closed cases than for the open cases because the injectors are unable to recover before the reflected wave's arrival.

Since the available constituents in the flow field available for the detonation waves to consume influences the wave speed, phase-averaged representations of the combustion front are characterized and presented in Figure 3.11. Broadband images from the window B region were phase-averaged into 100 divisions and consisted of at least 1,000 frames for which the dominant, right-running wave are present. First, the detonation front at the injection surface is located in each frame by utilizing the y-t plot in Figure 2.6b. Phase angles are then assigned to each column in each frame such that the detonation front is always at zero degrees. This assignment is performed for a column by temporally interpolating between the amount of time that has passed since a wave front has travelled past this column and the amount of time until the next wave front passes. For each division in phase angle, the corresponding column in each frame are averaged to produce the phase averaged image presented in Figure 3.11.

The detonation fronts from these phase averaged images are overlaid for direct comparison in Figure 3.12. These detonation fronts are distinguished by applying a marching squares edge detection to sobel-filtered phase averaged images. Case (i) in Figure 3.12 demonstrates a detonation wave that is attached to the injection surface because of a well-mixed flow field above the injection surface. The detonation front assumes a vertical and compact shape. However, as the equivalence ratio increases for the remainder of the open cases (ii) and (iii), the detonation front becomes further separated. This trend indicates that as the flow field becomes more fuel-rich and the fuel jet recovery time decreases, the detonation front must separate from the injection surface and travel further downstream so that it can propagate through a well-mixed flow field [35], [36]. As a result, the upper portion of the detonation front leads the wave and gives it the appearance of leaning forward.

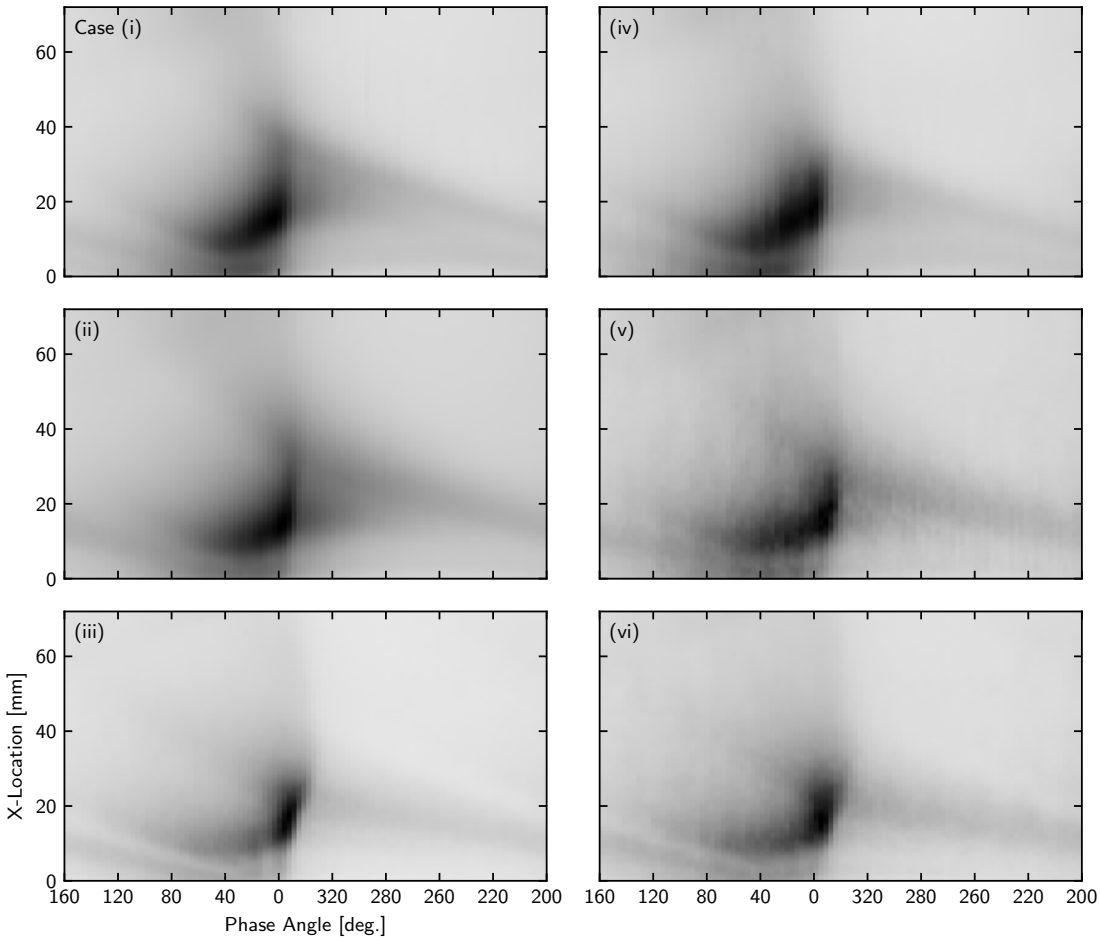

Figure 3.11. Phased averaged detonation front for each case.

This coupled phenomena between recovery time, equivalence ratio, and detonation wave propagation is consistent for closed cases (iv), (v), and (vi) as seen in Figure 3.12. Boundary conditions don't directly influence the detonation front contour because the dominant, right-running detonation waves are propagating through a region where the injectors have recovered. The fronts of the reflected, left-running waves are be expected to be altered in the zones where the injectors have yet to recover because the detonation front must separate from the injection surface to propagate further downstream in a region where burned products are mixed with un-burned reactants rather than along the injection surface through a flow field of burned products. However, it is for this reason that the reflected detonations don't emit sufficient light intensity to generate phase average images of the reflected wave

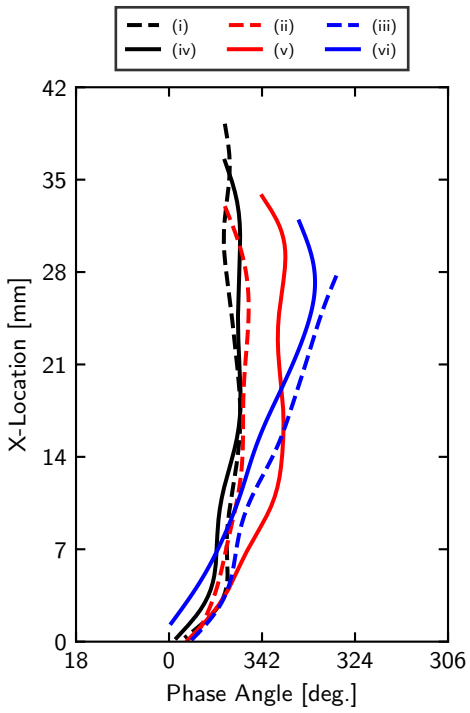

Figure 3.12. The fronts of the phased averaged detonations for open (dashed) and closed (solid) cases of fuel-lean (black), stoichiometric (red), and fuel-rich (blue) equivalence ratios.

in the window B region until they accelerate and amplify in the window A region before being reflected by the other closed boundary. Once the reflected wave propagates into the window A area, the local injectors have recovered and the left-running waves will assume fronts similar to those presented in Figure 3.12.

3.3 Amplification of Detonation Waves

In addition to influencing the acceleration of waves present in the LDC, the boundary conditions also impact the amplification of these waves as presented in Figure 3.13. The pressure fluctuation (blue) is determined for each high-frequency pressure sensor and the light intensity (green) is drawn from each PMT. These traces are then overlaid with the y-t plots derived from the broadband imaging taken in window A and window B. The pressure traces are de-trended with a high pass band filter and then both pressure and intensity signals are normalized with respect to the greatest global value collected by each sensor.

At locations where counter-propagating waves interact, the pressure fluctuation amplitude decreases which results in weaker waveforms. Greater light intensity corresponds with the steepening of the pressure wave form which indicates that shock coupled heat release is occurring in regions after the wave has accelerated beyond the acoustic speed of burned products.

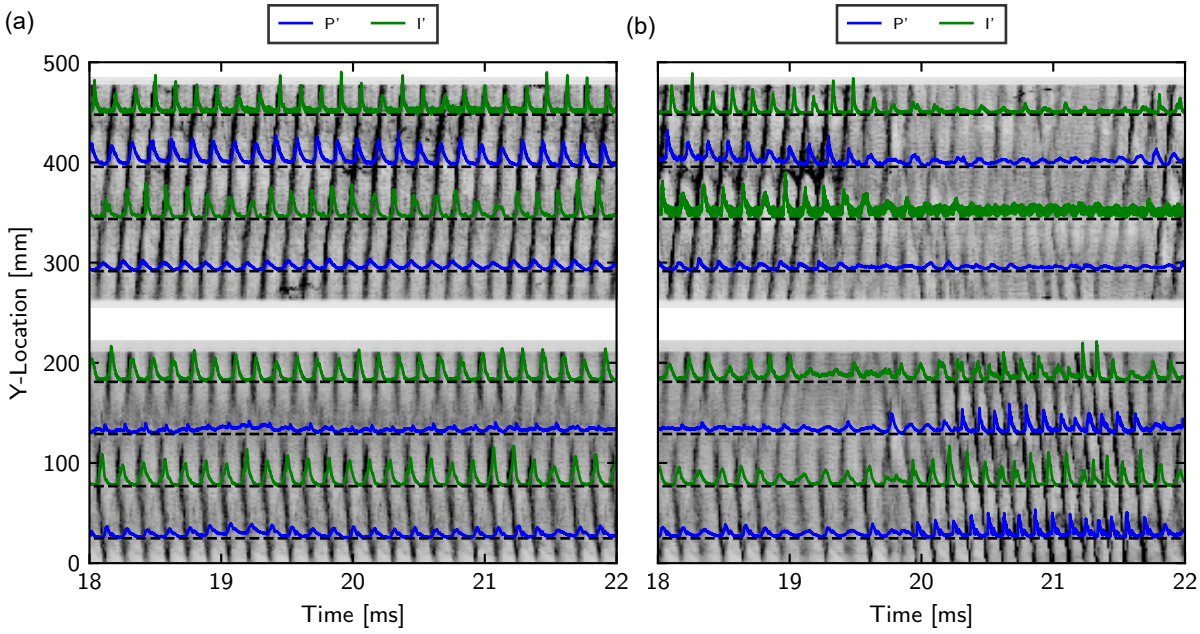

Figure 3.13. Pressure fluctuation (blue) and light intensity (green) in the combustion chamber for (a) Case (i) and (b) Case (iv).

The open case (i) seen in Figure 3.13a demonstrates that the stronger detonation wave travels from the closed-end (Y = 0 mm) to the open-end (Y = 540 mm) while a weaker combustion wave propagates counter to the stronger wave. For the closed case (iv) presented in Figure 3.13b, the direction of the dominant detonation wave alternates as indicated by the transition in amplification. Between 18 and 19 ms, the stronger wave amplifies from the left-end (Y = 0 mm) to the right-end (Y = 540 mm) as evident by the increase in pressure fluctuation and light intensity along the length of the combustor. Alternatively, between 20 and 22 ms, the pressure fluctuation and light intensity increasing from the right-edge to the left-edge which implies a transition in mode and the dominant detonation wave is now travelling leftward while the weaker wave is propagating rightward. For all open cases, the

dominant wave always propagates rightward while the direction of dominance alternates for all closed cases with no observed periodicity.

To further explore the relationship between the boundary condition and the amplification process, the coefficient of acoustic reflection for both conditions is estimated. The stainless steel plate placed for closed cases is 1.00 while the coefficient for the open cases, which are exposed to atmospheric conditions, varies with equivalence ratio as seen in Figure 3.14. To approximate the coefficient of reflection for open cases, the density and local speed of sound are calculated with Cantera from temperature and pressure traces in the fuel and oxidizer manifolds and their corresponding mass flow rates. These values are utilized to estimate the acoustic impedance of the incident or right-running detonation wave [42]–[44]. The incident wave then leaves the combustor through the open boundary into atmospheric conditions. Therefore, the density and speed of sound for the reflected wave are calculated assuming a flow field of air at atmospheric conditions (T = 294 K, P = 1 atm) to estimate the reflected wave's impedance. The ratio between the impedance of the reflected wave to the incident wave is referred to as the relative characteristic impedance, $r_{1,2}$, which is then used to approximate the coefficient of reflection according to Equation 3.1 [45].

$$\alpha_r = 1 - \left(\frac{r_{1,2} - 1}{r_{1,2} + 1}\right)^2 \tag{3.1}$$

From Figure 3.14, it can be observed that the coefficient of reflection decreases as equivalence ratio increases for open cases while the fuel jet recovery time also decreases. The frequency and number of waves increase to then consume the abundance of reactants since the recovery time has been shortened. As a result, the time for the reflected wave to arrive also decreases since the injectors recover relatively quickly. The reflected, left-running waves propagate sonically and don't amplify, but the right-running waves accelerate and amplify in the same direction as they travel from the closed-end to the open-end as seen in Figure 3.13a.

Meanwhile, for closed cases, the coefficient of reflection is consistently 1.00 for both boundaries independent of the equivalence ratio. Because the detonation wave is completely and immediately reflected into a flow field of burned products, the reflected wave is "suffo-

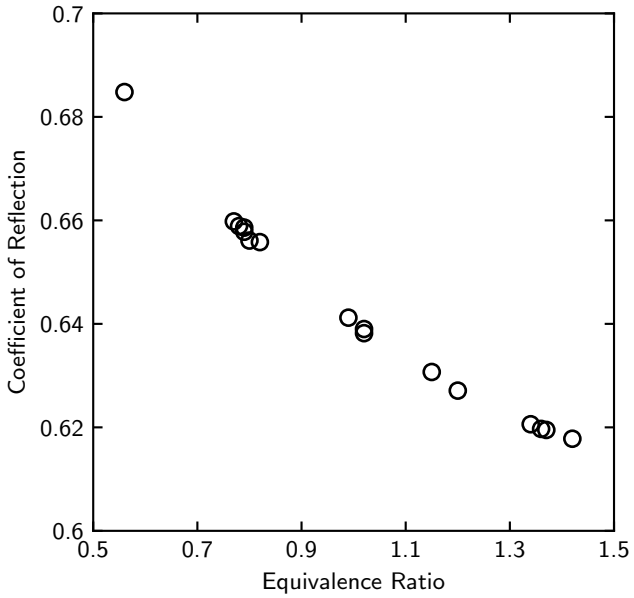

Figure 3.14. Coefficient of reflection for open cases.

cated" as demonstrated by less light intensity and pressure fluctuation for the right-running waves at the left-end and for left-running waves at the right-end in Figure 3.13b. The direction of amplification alternates between right-running and left-running waves as seen in Figure 3.13b but the direction of acceleration for right-running and left-running waves doesn't alternate as seen by the consistency between the streaks of waves in different modes. As previously discussed, right-running waves accelerate and amplify during periods of rightward dominance while left-running waves accelerate but never exceed the acoustic velocity of the burned products and don't amplify. During periods of leftward dominance, left-running waves accelerate and amplify while right-running waves accelerate but don't amplify. As a result, the direction of amplification isn't always the same direction as acceleration for closed cases.

3.4 Self-Excitation of Detonation Waves

To characterize the self-excitation of the combustion waves propagating in the combustor, the role of the closed boundary at Y = 0 mm and the subsequent circulation zone were observed by re-locating the boundary as discussed in Section 2.3. The interaction between

a self-excited detonation wave and this boundary are depicted in Figure 3.15. The schlieren and OH*-chemiluminescence images taken in window A during steady-state operation are overlaid for one cycle of a left-running detonation wave such that the schlieren image is in a grey-scale and the OH*-chemiluminescence is in a red-scale. Approximately 10.41 μs elapses between each frame for this case which operated at similar conditions to case (i) with an equivalence ratio of 0.80, a mass flux of 121 kg/(s.m^2), and closed-open boundaries.

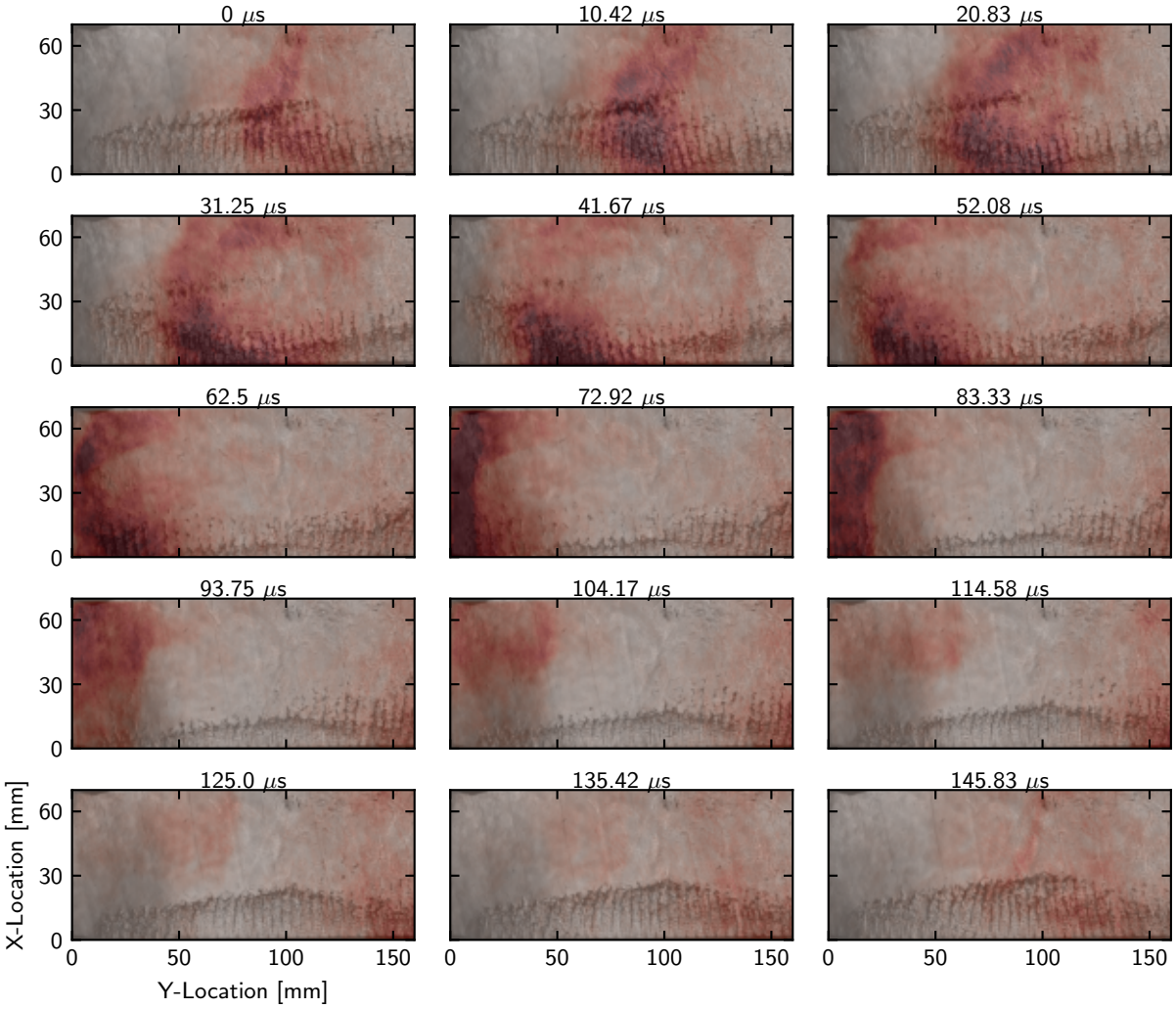

Figure 3.15. Schlieren (grey) and OH*-chemiluminescence (red) of a left-running detonation wave interacting with the closed boundary at Y = 0 mm.

As seen in the frame at 0 μs, the left-running wave approaches the boundary at Y = 0 mm. In frame 72.92 μs, the wave impacts the boundary and is reflected into a right-running

wave that leaves the field of view after frame 145.83 μs. Therefore, this closed boundary serves as a reflective boundary. Waves in open cases accelerate and amplify from the closed boundary (Y = 0 mm) to the open boundary (Y = 540 mm) as depicted in Figures 3.9 and 3.13, respectively, which indicate that the detonation waves are originating from the closed boundary. However, waves aren't emanating from this closed boundary since reactants aren't accumulating in this re-circulation zone to support a source for new waves. If this boundary did serve as the excitation source, flame holding would be observed at Y = 0 mm in Figure 3.15. Rather, flame instabilities generate pulsations which non-linearly and gradually amplify and transition into transverse waves [16]. These waves then accelerate and further amplify into detonation waves as established in Sections 3.2 and 3.3.

4. SUMMARY

In this study, the propagation of self-excited combustion waves are characterized in a gaseous non-premixed, linear detonation combustor. High-fidelity diagnostics such as HF sensors, schlieren, OH*-chemiluminescence, and broadband imaging are deployed to observe the non-linear global wave dynamics in the combustor. The acceleration, amplification, and self-excitation of these waves are then further investigated.

First, the presence of periodic, counter-propagating waves are established in this experimental combustor with y-t plots extracted from the broadband imaging taken of the aft end of the device. These waves self-excite with a kilohertz-rate cycle frequency that increases with the equivalence ratio. The number of detonation waves also increases as cycle frequency and equivalence ratio increase. However, stoichiometric open cases and fuel-lean ($\phi = 0.80$) closed cases exhibit the fewest number of waves and the lowest pressure fluctuations. As a result, these global combustor behaviors are non-linearly coupled with other mechanisms such as mixing, boundary conditions, and wave self-excitation, acceleration, and amplification.

The combustor was modified to relocate the circulation zone near the closed boundary at Y = 0 mm to be optically accessible with high-speed diagnostics. It was determined that reactants weren't accumulating in this zone and no flame holding was present on this surface. Therefore, closed boundaries don't serve as a source of excitation for new combustion waves in the combustor. Instead, closed boundaries behave as a reflective surface for self-excited and self-sustained waves that develop from flame instabilities.

An algorithm was developed to calculate the wave speed of propagating waves from the y-t plots derived from broadband images of the combustor's aft-end. For open cases, the right-running waves accelerate along the length of the combustor to supersonic speeds relative to the acoustic velocity of burned products. These waves then reflect off an open boundary with a coefficient of reflection that decreases as equivalence ratio increases. The partially reflected waves re-enter the combustor with less strength after the injectors have recovered. Since a sufficient amount of time has passed between the arrival of the incident waves and the departure of the reflected waves, as seen in the y-t plots, the window B region is filled with fresh reactants for the reflected waves to consume. The reflected waves propagate sonically

as left-running waves until they are reflected by the closed boundary into right-running waves once again. The direction of acceleration and amplification for open cases is from the closed-boundary to the open-boundary as exemplified by the increase in pressure fluctuation and wave steepening along the length of the combustor.

For cases with closed boundaries, the right-running waves accelerate along the length of the combustor and become supersonic before reaching the closed boundary at Y = 540 mm. These waves are then immediately and completely reflected into a region filled with burned products. Because the coefficient of reflection for closed boundaries is 1.00, an insufficient amount of time has passed between the incident and reflected waves for the fuel injectors to be able to recover. As a result, the window B region is still filled with the burned products from the incident waves and the reflected waves are suffocated. Consequently, the speed of the reflected waves is less than the incident waves until the reflected waves accelerate. However, the left-running wave don't exceed the local acoustic sonic velocity before being reflected by the closed boundary at Y = 0 mm for which the process repeats itself. Although the left-running and right-running consistently experience acceleration in both directions, the direction of amplification alternates with no periodicity.

5. RECOMMENDATIONS

It is recommended to deploy planar laser induced fluorescence (PLIF) in the combustor to quantify the local mixing field near the closed and open boundaries. This information will give insight into the impact boundary conditions have on the flow field before and after counter-propagating waves. The reflected waves propagate through a flow field of fresh reactants mixed with burned products from the passage of the incident waves that are re-circulating in the combustor. By investigating the composition and state of flow near the boundaries, the influence these geometric boundaries have on chemical timescales will be better understood. Additionally, the local speed of sound will be able to be calculated from the constituents present in the local flow field. For this work, the local acoustic velocity was estimated for fresh reactants and burned products. The more conservative value between the two estimations was selected for comparison with the calculated wave speeds. A quantified flow field will yield a more accurate criterion for which wave speed can be compared [15].

Further modifications of the combustor geometry are also recommended to understand it's influence on wave speed and strength. For the work presented, the combustor's transverse (Y-direction) length was shortened from 610 mm to 540 mm by inserting stainless steel blocks before the window A region. This modification was made to support advanced diagnostics in the region near this closed boundary. Although this modification didn't have a great impact on the global wave dynamics in the combustor, larger modifications in the length-to-width ratio of the combustor may. By lengthening or shortening the combustor while maintaining the width, the waveguide path-length will be altered which may impact cell size [46] and consequently, the global wave dynamics as to promote wave acceleration and amplification. As a result, advanced diagnostics such as schlieren and OH*-chemiluminescence should be utilized near the boundaries and throughout the channel to investigate different combustor length-to-width ratios.

REFERENCES

[1] E. Wintenberger and J. E. Shepherd, "The stagnation hugoniot analysis for steady combustion waves in propulsion systems," *Journal of Propulsion and Power*, vol. 22, pp. 835–844, 4 2006. DOI: https://doi.org/10.2514/1.12779.

[2] F. A. Bykovskii, S. A. Zhadan, and E. F. Vedernikov, "Continuous spin detonations," *Journal of Propulsion and Power*, vol. 22, pp. 1204–1216, 6 2006. DOI: https://doi.org/10.2514/1.17656.

[3] J. Lee, *The detonation phenomenon*. Cambridge University Press, 2014.

[4] F. K. Lu and E. M. Braun, "Rotating detonation wave proulsion: Experiemntal challenges, modeling, and engine concepts," *Journal of Propulsion and Power*, vol. 30, pp. 1125–1142, 5 2014. DOI: https://doi.org/10.2514/1.b34802.

[5] P. Wolański, "Application of the continuous rotating detonation to gas turbine," *Applied mechanics and materials*, vol. 782, pp. 3–12, 2015. DOI: 10.4028/www.scientific.net/AMM.782.3.

[6] S. M. Frolov, V. S. Aksenov, A. V. Dubrovskii, V. S. Ivanov, and I. O. Shamshin, "Energy efficiency of a continuous-detonation combustion chamber," *Combustion, Explosion, and Shock Waves*, vol. 51, pp. 232–245, 2 2015. DOI: https://doi.org/10.1134/S0010508215020070.

[7] P. Wolański, *Detonative propulsion*, Nov. 1, 2012. DOI: https://doi.org/10.1016/j.proce.2012.10.005.

[8] W. H. Heiser and D. T. Pratt, "Thermodynamic cycle analysis of pulse detonation engines," *Journal of Propulsion and Power*, vol. 18, pp. 68–76, 2002. DOI: https://doi.org/10.2514/2.5899.

[9] K. Schwinn, R. Gejji, B. Kan, S. Sardeschmukh, S. Heister, and C. D. Slabaugh, "Self-sustained, high-frequency detonation wave generation in a semi-bounded channel," *Combustion and Flame*, vol. 193, pp. 384–396, 2018. DOI: https://doi.org/10.1016/j.combustflame.2018.03.022.

[10] D. Schwer and K. Kailasanath, "Fluid dynamics of rotating detonation engines with hydrogen and hydrocarbon fuels," *Proceedings of the Combustion Institute*, vol. 34, pp. 1991–1998, 2 2013. DOI: https://doi.org/10.1016/j.proci.2012.05.046.

[11] J. Anderson, *Modern compressible flow: with historical perspective*, 3rd ed. McGraw-Hill Higher Education, 2002.

[12] Q. Li, P. Liu, and H. Zhang, "Further investigations on the interface instability between fresh injections and burnt products in 2-d rotating detonation," *Computers and Fluids*, vol. 170, pp. 261–272, 2018. DOI: https://doi.org/10.1016/j.compfluid.2018.05.005.

[13] P. Liu, Q. Li, Z. Huang, and H. Zhang, "Interpretation of wake instability at slip line in rotating detonation," *International Journal of Computational Fluid Dynamics*, vol. 32, pp. 379–394, 8–9 2018. DOI: https://doi.org/10.1080/10618562.2018.1533634.

[14] R. Bleumner, M. D. Bohon, C. O. Paschereit, and E. J. Gutmark, "Effect of inlet and outlet boundary conditions on rotating detonation combustion," *Combustion and Flame*, vol. 216, pp. 300–315, 2020.

[15] J. Koch, M. Kurosaka, and C. Knowlen, "Mode-locked rotating detonation waves: Experiments and a model equation," *Physical Review E.*, vol. 101, 2020. DOI: https://doi.org/10.1103/PhysicRevE.101.013106.

[16] V. N. Gamezo, A. Y. Poludnenko, E. S. Oran, and F. A. Williams, "Transverse waves resulting from pulsating instability of two-dimensional flames," *Combustion and Flame*, vol. 161, pp. 950–957, 2014. DOI: https://doi.org/10.1016/j.combustflame.2013.09.027.

[17] T. C. Rathsack, J. R. Burr, B. R. Bigler, and J. W. Bennewitz, *Analysis of single wave behavior in a linear detonation channel using injector plane oriented direct imaging*, Jan. 1, 2021. DOI: https://doi.org/10.2514/6.2021-1380.

[18] M. Yamaguchi, T. Taguchi, K. Matsuoka, *et al.*, *Investigation of combustion modes and pressure of reflective shuttling detonation combustor*, Sep. 1, 2020. DOI: https://doi.org/10.1016/j.proci.2020.07.064.

[19] R. Bleumner, M. D. Bohon, C. O. Paschereit, and E. J. Gutmark, "Counter-rotating wave mode transition dynamics in an rdc," *International Journal of Hydrogen Energy*, vol. 44, pp. 7628–7641, 14 2019. DOI: https://doi.org/10.1016/j.ijhydene.2019.01.262.

[20] J. W. Bennewitz, B. R. Bigler, J. J. Pilgram, and W. A. H. Jr., "Modal transitions in rotating detonation rocket engines," *International Journal of Energetic Materials and Chemical Propulsion*, vol. 18, pp. 91–109, 2 2019.

[21] H. Meng, Q. Zheng, C. Weng, *et al.*, "Propagation mode analysis of rotating detonation waves fueled by liquid kerosene," *Acta Astronautica*, vol. 187, pp. 248–258, 2021. DOI: https://doi.org/10.1016/j.actaastro.2021.06.043.

[22] J. Crane, X. Shi, J. T. Lipkowicz, A. M. Kempf, and H. Wang, *Geometric modeling and analysis of detonation cellular stability*, Sep. 1, 2021. DOI: https://doi.org/10.1016/j.proci.2020.06.278.

[23] M. Weilenmann and N. Noiray, "Experiments on sound reflection and production by choked nozzle flows subject to acoustic entropy waves," *Journal of sound and vibration*, vol. 4925, 2021. DOI: https://doi.org/10.1016/j.jsv.2020.115799.

[24] G. Ciccarelli and S. Dorofeev, "Flame acceleration and transition to detonation in ducts," *Progress in Energy and Combustion Science*, vol. 34, pp. 499–550, 4 2008. DOI: https://doi.org/10.1016/j.pecs.2007.11.002.

[25] N. Noiray and B. Schuermans, "Deterministic quantities characterizing noise driven hopf bifurcations in gas turbine combustors," *International Journal of Non-Linear Mechanics*, vol. 50, pp. 152–163, 2013. DOI: https://doi.org/10.1016/j.jnonlinmec.2012.11.008.

[26] E. S. Oran and J. H. Gardner, "Chemical-acoustic interactions in combustion systems," *Progress in energy and combustion science*, vol. 11, pp. 253–276, 1985.

[27] K. S. Schwinn, "Characteristics of periodic, self-sustained detonation generation in an rde analogue," Ph.D. dissertation, Purdue University, 2021.

[28] I. Q. Andrus, P. I. . King, M. D. Polanka, F. R. Shcuauer, and J. L. Hoke, "Design of a premixed fuel – oxidizer system to arrest flashback in a rotating detonation engine," *Journal of Propulsion and Power*, vol. 33, pp. 1063–1073, 5 2017. DOI: https://doi.org/10.2514/1.B36259.

[29] R. M. Gejji, I. V. Walters, A. Lemcherfi, S. V. Sardeshmukh, S. D. Heister, and C. D. Slabaugh, "Transducer installation effects on pressure measurements in pgc devices," *56th AIAA Aerospace Sciences Meeting*, 2018. DOI: https://doi.org/10.2514/6.2018-0158.

[30] K. Schwinn, B. Kan, S. Sardeshmukh, R. Gejji, S. Heister, and C. D. Slabaugh, *Self-excited, multi-khz dynamics in a linear semi-bounded detonation channel*, Jan. 1, 2017. DOI: https://doi.org/10.2514/6.2017-0375.

[31] G. S. Settles, *Schlieren and shadowgraph techniques: visualizing phenomena in transparent media*. Springer-Verlag Berlin Heidelberg, 2001, pp. 42–46.

[32] K. Schwinn, R. Gejji, and C. D. Slabaugh, *The effects of chemical kinetics on detonation propagation in an unwrapped rde*, Aug. 16, 2019. DOI: https://doi.org/10.2514/6.2019-3951.

[33] J. Bennewitz, B. Bigler, W. Hargus, S. Danczyk, and R. Smith, *Characterization of detonation wave propagation in a rotating detonation rocket engine using direct high-speed imaging*, Jul. 1, 2021. DOI: https://doi.org/10.2514/6.2018-4688.

[34] C. L. Journell, R. M. Gejji, I. V. Walters, A. I. Lemcherfi, C. D. Slabaugh, and J. B. Stout, "High-speed diagnostics in a natural gas-air rotating detonation engine," *Journal of Propulsion and Power*, vol. 36, 4 2020. DOI: https://doi.org/10.2514/1.B37740.

[35] Z. M. Ayers, A. Lemcherfi, E. W. Plaehn, *et al.*, "Simultaneous 100–khz acetone planar laser-induced fluorescence and oh* chemiluminescence in a linear non-premixed detonation channel," *Combustion and Flame*, 2022.

[36] A. Lemcherfi, R. Gejji, Z. M. Ayers, *et al.*, "Effect of injection dynamics on detonation wave propagation in a linear detonation combustor," *Proceedings of Combustion Institute*, vol. 39, 2022.

[37] A. S. of Mechanical Engineers, "Measurement of gas flow by means of critical flow venturis and critical flow nozzles," *ASME MFC-7-2016*, 2016.

[38] S. J. Kline and F. A. McClintock, "Describing uncertainties in single-sample experiments," *ASME*, vol. 75, pp. 3–8, 1952.

[39] R. J. Moffat, "Describing the uncertainties in experimental results," *Experimental Thermal and Fluid Science*, vol. 1, pp. 3–17, 1 1988. DOI: https://doi.org/10.1016/0894-1777(88)90043-X.

[40] I. V. Walters, R. M. Gejji, S. D. Heister, and C. D. Slabaugh, "Flow and performance analysis of a natural gas-air rotating detonation engine with high-speed velocimetry," *Combustion and Flame*, vol. 232, 2021. DOI: https://doi.org/10.1016/j.combustflame.2021.111549.

[41] C. Robbe, N. Nsiampa, A. Oukara, and A. Papy, "Quantification of the uncertainties of high-speed camera measurements," *International Journal of Metrology and Quality Engineering*, vol. 5, 201 2014. DOI: http://dx.doi.org/10.1051/ijmqe/2014007.

[42] R. R. Nourgaliev, S. Y. Sushchikh, T. N. Dinh, and T. G. Theofanous, "Shock wave refraction patterns in interfaces," *International journal on multiphase flow*, vol. 31, pp. 969–995, 9 2005. DOI: https://doi.org/10.1016/j.ijmultiphaseflow.2005.04.001.

[43] P. B. Subrahmanyam, R. I. Sujith, and T. C. Lieuwen, "A family of exact transient solutions for acoustic wave propagation in inhomogeneous non-uniform area ducts," *Journal of sound and vibration*, vol. 240, pp. 705–715, 4 2001.

[44] D. C. Pack, "The reflection and transmission of shock waves i: The reflection of a detonation wave at a boundary," *The Philosophical Magazine: A Journal of Theoretical Experimental and Applied Physics*, vol. 2, pp. 182–188, 14 1956. DOI: https://doi.org/10.1080/14786435708243807.

[45] L. E. Kinsler and A. R. Frey, *Fundamentals of acoustic*. John Wily and Sons Inc., 1950, ch. 6, pp. 142–144.

[46] H. Nakayama, T. Moriya, J. Kasahara, A. Matsuo, Y. Sasamoto, and I. Funaki, "Stable detonation wave propagation in rectangular-cross-section curved channels," *Combustion and flame*, vol. 159, pp. 859–869, 2 2012. DOI: https://doi.org//10.1016/j.combustflame.2011.07.022.

PUBLICATION

Journal Publication

- D. R. Jackson, M. D. Frederick, R. M. Gejji, J. W. Bennewitz, J. Burr, and C. D. Slabaugh, "Characteristics of Self-Excited Wave Propagation in a Non-Premixed Linear Detonation Combustor," (manuscript in preparation for submission to Combustion and Flame), 2022